DOI: 10.1002/chem.200802329

# Peptide-Coated Silver Nanoparticles: Synthesis, Surface Chemistry, and pH-Triggered, Reversible Assembly into Particle Assemblies

**Philipp Graf,[a] Alexandre Mantion,*[a, e, f] Annette Foelske,[b] Andriy Shkilnyy,[c, d] Admir Mašić,[d] Andreas F. Thünemann,[e] and Andreas Taubert*[a, c, d]**

**Abstract:** Simple tripeptides are scaffolds for the synthesis and further assembly of peptide/silver nanoparticle composites. Herein, we further explore peptide-controlled silver nanoparticle assembly processes. Silver nanoparticles with a pH-responsive peptide coating have been synthesized by using a one-step precipitation/coating route. The nature of the peptide/silver interaction and the effect of the peptide on the formation of the silver particles have been studied via UV/Vis, X-ray photoelectron, and surface-enhanced Raman spectroscopies as well as through electron microscopy, small angle X-ray scattering and powder X-ray diffraction with Rietveld refinement. The particles reversibly form aggregates of different sizes in aqueous solution. The state of aggregation can be controlled by the solution pH value. At low pH values, individual particles are present. At neutral pH values, small clusters form and at high pH values, large precipitates are observed.

**Keywords:** hybrid materials · nanoparticles · oligopeptides · pH · silver

## Introduction

Metal nanoparticles, in particular silver nanoparticles, have attracted attention because of their interesting optical properties.[1] Silver nanoparticles have also been studied as biomarkers and sensors[2] or in antibiotic applications.[3,4] Now, metal-nanoparticle synthesis is well established.[5,6] Electromagnetic radiation,[7–11] dimethylformamide (DMF),[12] ascorbate,[13–15] and citrate[16–19] are common reducing agents for silver salts. Ascorbate and citrate have become popular for their "green" connotation, but they also lead to uniform nanoparticles,[20] including nanorods,[21] core–shell structures,[22,23] and polyamine-[24] and polysulfonate-stabilized[14,25] nanoparticles. Current research focuses on factors that control the shape, size, and size distribution of the particles by using ascorbate.[26,27] Reduction of silver ions with DMF is less studied, but also yields well-defined silver nanoparticles.[12,28]

For many applications, nanoparticle dispersions in water are desirable. Among others, nanoparticle dispersions have been stabilized with water-soluble polymers,[29–32] dendritic stabilizers,[33,34] thiols,[35] cyclodextrins,[36] and genetically engineered proteins.[37] Proteins are interesting stabilizers because they can combine a wide range of properties in one molecule, such as communication with biology, stimuli responsiveness, and tailored interaction with a nanoparticle surface. As a result, protein/nanoparticle hybrid structures are potentially interesting for the fabrication of (biomimetic) advanced functional materials. However, proteins are often difficult to process, modify, and obtain in large quantities.

Peptides can be viewed as simple variants of proteins. Depending on the amino acid sequence, they can be acidic,

[a] P. Graf, Dr. A. Mantion, Prof. Dr. A. Taubert
Department of Chemistry, Klingelbergstrasse 80
University of Basel, 4056 Basel (Switzerland)
Fax: (+49) 331-977-5773
E-mail: alexandre.mantion@bam.de
ataubert@uni-potsdam.de

[b] Dr. A. Foelske
Electrochemistry Laboratory, Paul Scherrer Institute
5232 Villigen (Switzerland)

[c] Dr. A. Shkilnyy, Prof. Dr. A. Taubert
Institute of Chemistry, University of Potsdam
14476 Golm (Germany)

[d] Dr. A. Shkilnyy, Dr. A. Mašić, Prof. Dr. A. Taubert
Max-Planck-Institute of Colloids and Interfaces
14476 Golm (Germany)

[e] Dr. A. Mantion, Prof. Dr. A. F. Thünemann
BAM Federal Institute for Materials Research and Testing
Richard-Willstaetter-Strasse 11, 12489 Berlin (Germany)

[f] Dr. A. Mantion
Current address:
BAM Federal Institute for Materials Research and Testing
Richard-Willstaetter-Strasse 11, 12489 Berlin (Germany)
Fax: (+49) 30-8104-1137

   

basic, hydrophilic, or hydrophobic. In contrast to proteins, they are usually available on the gram scale. As a result, peptides are attractive building blocks for advanced materials.[38–40]

Despite these interesting properties, however, little is known on the synthesis and properties of metal nanoparticle/peptide hybrids. Naik et al. have described the growth of nano-objects in the presence of small peptides.[41] The peptides are often based on L-tryptophane[42,43] and L-tyrosine[44] because of their propensity to form organogels and to be redox active.

Similarly, little is known on how peptides control the assembly of nanoparticles. The assembly of thiol- or polymer-stabilized metal nanoparticles is rather well understood,[45–50] but there are comparatively few data on how peptides control the self-assembly of metal particles. Correspondingly, little is known on how the peptides affect the properties of the resulting peptide/inorganic hybrid material.[51–54] Understanding and controlling the response of hybrid nanoparticles and being able to regulate their assembly is, however, crucial for the design of novel materials with specific properties such as a well-defined optical response.

As a result, there is a need to further study the synthesis, structure, and behavior of peptide-functionalized metal nanoparticles as building blocks for complex materials. The current study presents an in-depth investigation of a peptide/metal nanoparticle model system. The model system consists of silver nanoparticles coated with a pH-responsive hexapeptide (Scheme 1). The goal of the study is to 1) determine the exact nature of the silver nanoparticle surface, 2) the type of interaction between the silver nanoparticle surface and the peptide, and 3) the self-assembly behavior versus the pH of the nanoparticle dispersion.

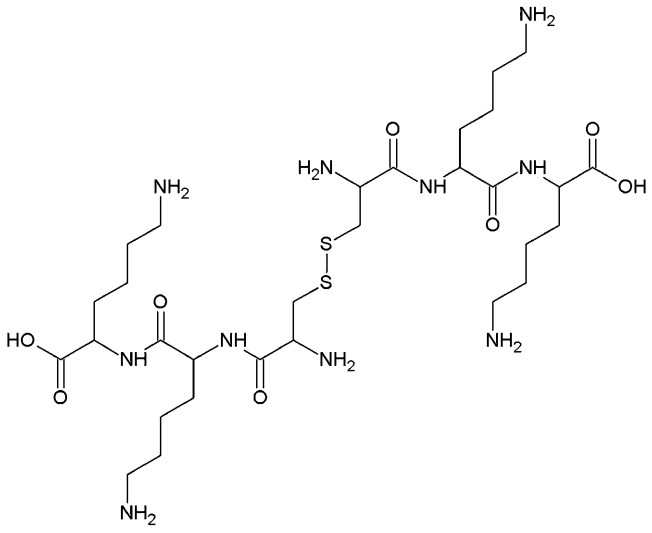


Scheme 1. Peptide **4** used in this study. All amino acids are L-amino acids. The neutral form of the peptide is shown. The peptide sequence is Lys-Lys-Cys (KKC). The two sequences are connected through disulfide bridge (-S–S-). Peptide **4** was prepared from precursors **1**, **2**, and **3** (see the Experimental Section).

## Results

**Pure peptide**: Figure 1 shows representative IR spectroscopy data of the pure peptide **4**. IR spectra show overlapping

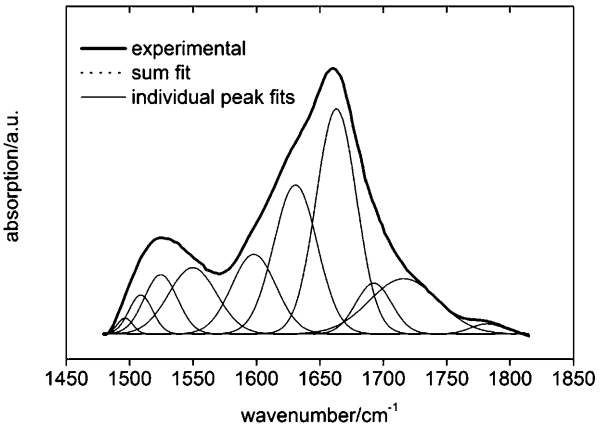


Figure 1. Deconvoluted IR spectrum (diagnostic region) of the pure peptide. The sum fit overlaps with the experimental curve.

bands in the region between 1550 and 1800 $cm^{-1}$, which is the diagnostic region for the secondary structure in peptides. Peak deconvolution indicates amide I bands ν(C=O) at 1663 $cm^{-1}$ and 1692 $cm^{-1}$ and an amide II band at 1550 $cm^{-1}$. IR suggests that in the solid state (the powder), the peptide adopts a $3_{10}$ helix[55–57] as suggested by the amide I and amide II bands. A β-sheet turn-type secondary structure[58] cannot be excluded, but the signals around 1631 $cm^{-1}$ are obscured by the presence of ν(N–H)[59] and may only be detected by X-ray diffraction or 2D IR spectroscopy. Besides the amide I and II bands, symmetric and asymmetric ν(N–H) bending bands at 1630 $cm^{-1}$ and 1524 $cm^{-1}$, a trifluoroacetic acid (TFA) carboxylate ν(C=O) band at 1597 $cm^{-1}$, carboxylic acid bands (terminal carboxylic acid) at 1716 $cm^{-1}$ and 1782 $cm^{-1}$,[59] are also observed. A shoulder at 3280 $cm^{-1}$ is due to amide A bands and indicates the presence of a β sheet.[58]

Figure 2 shows an X-ray diffraction (XRD) pattern of the peptide powder. It shows two peaks at 20.11° (d spacing of 4.41 Å) and at 55.12° (d spacing of 1.66 Å). The first peak is broad. It is attributed to a β-sheet motive or, more generally, an intermolecular β turn.[58] The second peak is consistent with an intramolecular motive of a $3_{10}$ structure.[60] XRD thus supports IR spectroscopy in that in both cases, β-turn motives are found.

**Peptide-modified silver particles**: Sample P1 was prepared at pH 3, P2 at pH 7, and P3 at pH 9 (see the Experimental Section for details). Figure 3 shows a representative XRD pattern of P1. The reflections can be assigned to cubic face-centered metallic silver (Joint Committee of Powder Diffraction Standards (JCPDS) file 04–0783). The reflections are broad, indicating the presence of small particles. Rietveld refinement (Table 1) further confirms this as for all *hkl*

  

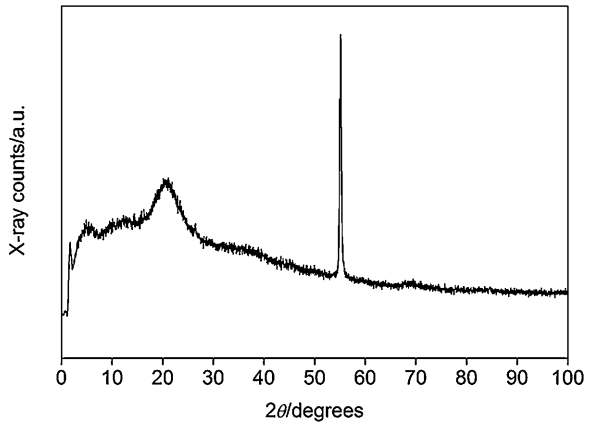


Figure 2. XRD pattern of the pure peptide.

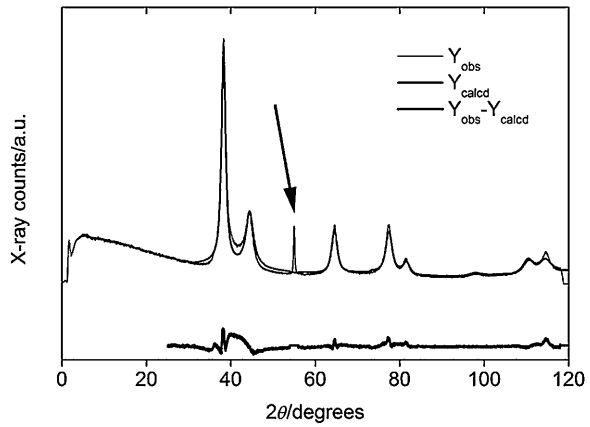


Figure 3. XRD pattern of P1 and corresponding Rietveld refinement. Arrow denotes the extra reflection at 54.94° as mentioned in the text.

Table 1. Crystallite sizes from Rietveld analysis.[a]

| (*hkl*) | P1 | P2 | P3 |
|---|---|---|---|
| (111) | 55 | 54 | 73 |
| (200) | 30 | 31 | 43 |
| (220) | 55 | 50 | 76 |
| (311) | 61 | 58 | 85 |
| (222) | 55 | 54 | 74 |
| (400) | 30 | 31 | 43 |
| (331) | 57 | 53 | 78 |
| (420) | 57 | 54 | 80 |
| average size (anisotropy) | 50 (11.44) | 48 (10.20) | 69 (15.44) |

[a] Sizes are in Ångstroms.

values, particle sizes below 15 nm are found. The ratio of the intensities (200)/(111) and (220)/(111) of our particles is between 0.35 and 0.44 or 0.22 and 0.26, respectively. This is roughly consistent with the JCPDS values, which are 0.40 and 0.25, respectively. This suggests that the particles are approximately spherical, but may be distorted somewhat. The bump in the residual curve of the Rietveld refinement between 38° and 45° is presumably due to an amorphous contribution of the peptide on the particle surface. Finally, there is also an extra reflection at 54.94°, which is not due to silver. Comparison with Figure 2 shows that this reflection can be assigned to the peptide.

Table 2 shows the shift of the (311) and (420) reflections compared with the particle preparation conditions with respect to their position in bulk, single crystalline silver

Table 2. Shift of (420) and (311) position in $2\theta$ [°] as a function of the synthesis pH value.[a]

| Reflection | P1 | P2 | P3 |
|---|---|---|---|
| (331) | 0.28 | 0.48 | −0.07 |
| (420) | −0.31 | 0.02 | −0.12 |

[a] Shifts are given with respect to the bulk silver structure (JCPDS 04–0783).

(JCPDS 04–0783). Shifts can be up to 0.5° $2\theta$, as revealed by Rietveld refinement. These shifts are rather large. The shifts are larger for (331) than (420). Overall, the shifts are most prominent for P1, which suggests that the crystal structure of P1 is the least close to bulk silver. This is interesting, because the crystallite sizes (Table 1) of P1 and P2 are essentially the same. As a result, this suggests that, possibly, there are surface effects contributing to a more distorted structure in P1. A more detailed discussion of this behavior is, however, complicated by the fact that the shifts in Table 2 are also affected by the amount of ligand on the surface and by the fact that there is also evidence for residual ascorbate on the particle surface (see below).

The crystal structure of P3 is more closely related to bulk silver than the others, as the shifts are rather limited. By using the microfacet[61] and step notation, the (331) reflection can be rewritten as $3(111)\times(11-1)$. This corresponds to a three-atom (111) terrace and one-atom (11−1) step in face-centered cubic crystal structures. Similarly, the (420) reflection can be rewritten as $Ag(S)\text{-}2\times(100)+1\times(111)+1\times(11-1)$, which corresponds to a kinked terrace. Both are indicating that high index lattice planes interact with the peptide disulfide bond or a thiol generated in situ. A similar behavior has been reported for gold nanoparticles that consist of 102 gold atoms and 44 *p*-mercaptobenzoic acid molecules.[62] Furthermore, Gaultier and Buergi[63] showed that chiral inversion of CD spectra of (thiol-modified) gold nanoparticles only happens if the gold crystal structure adapts so that it can present the ligand for maximal chemical interaction, namely adopts the chirality of the substrate. As a result, our data suggest that already a very simple peptide can significantly shift the fine structure of the crystal at its interface.

Aside from the silver reflections, XRD (Figure 3) also shows an additional peak at 54.94° (d spacing = 1.66 Å). This reflection is due to the helical pitch in the $3_{10}$ structure that is adopted by the peptide present on the particle. Interestingly, XRD suggests that the β-sheet component is lost when the peptide is adsorbed on the metallic surface. This can be concluded from the loss of the broad peak that is observed in the neat peptide at 20.11° (Figure 2).

  

Figure 4 shows representative transmission electron microscopy (TEM) images of the particles. Sample P1 (prepared at pH 3) and P2 (prepared at pH 7) are essentially identical, that is, in both cases roughly spherical particles

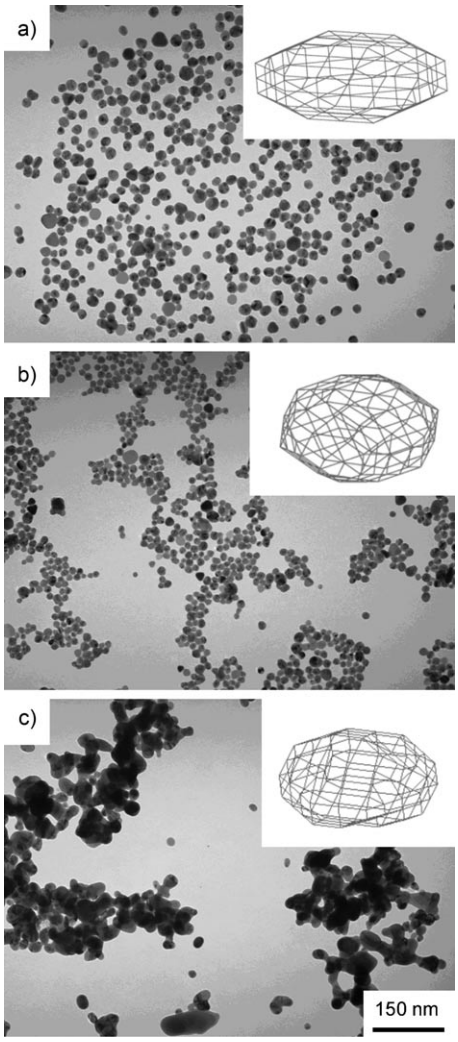


Figure 4. TEM images of a) P1 prepared at pH 3, b) P2 prepared at pH 7, and c) P3 prepared at pH 9. Insets are primary particle shapes (oblates) generated from XRD and Rietveld data via GFourier.[64] The scale bar applies to all images.

with diameters of $18.9 \pm 3.9$ nm (P1) and $15.4 \pm 5.0$ nm (P2) form. Both samples contain a few particles at the larger end of the size distribution that appear triangle-like. Unlike P1 and P2, P3 (prepared at pH 9) contains larger particles with a variety of shapes, including rod-like or elongated particles. These findings are different from results by Sondi et al.,[14] who showed that the higher the acidity of the starting silver solution, the bigger the particles are. However, as their protocol does not involve peptides, it is difficult to draw further conclusions.

Comparison of the XRD and TEM data suggests that, in spite of their small sizes, the particles (P3 in particular) are not single crystals but consist of a few smaller crystallites. Although XRD finds sizes around 2 to 5 nm, TEM finds particle sizes in the range of approximately 10–50 nm. Furthermore, the reconstructed primary particle shapes (crystallite shapes, see insets in Figure 4) only match the shapes of P1 and P2, but not P3.

Figure 5 shows representative IR spectra of the pure peptide and P1. The spectra of P1, P2, and P3 have very simple

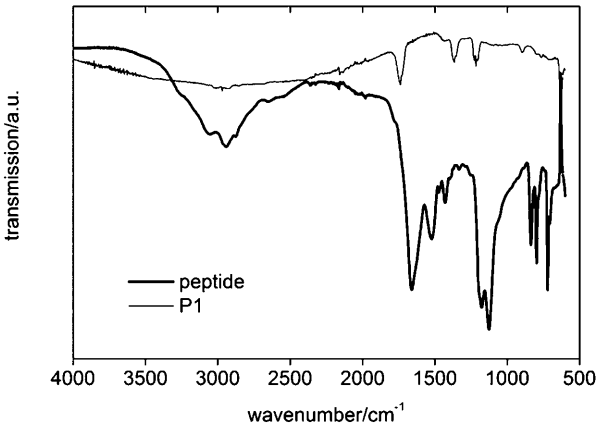


Figure 5. IR spectra of neat peptide **4** as a TFA salt and P1, respectively. The spectra for P1, P2, and P3 are virtually indistinguishable.

structures when compared with the original peptide. The only visible bands in the carbonyl region are at 1735 $cm^{-1}$ and 1212 $cm^{-1}$. They can be assigned to $\nu$(C=O) and $\nu$(C–O), respectively, from residual ascorbic acid adsorbed on the surface, remains of oxidized ascorbic acid, or the peptide carboxylic acid. Other vibrations are due to the aliphatic chain of the peptide and, again, some residues of the ascorbic acid and its oxidized form, mainly $\delta(CH_2)$, $\nu$(C–H), and $\nu$(N–H) at around 1200 to 1300 $cm^{-1}$ and 3000 $cm^{-1}$, respectively.

The lack of further signals is not surprising as the silver surface interferes with the IR spectra of bound molecules. The absence of further signals indicates that the peptide is close to the particle surface and the dipolar transition moments are parallel to the surface for the amide-bond transition. This in turn suggests that the amide bonds are parallel to the particle surface, which indicates that the peptides form a brush-like structure on the particle surface. They are thus not able to interact with the electric field present at the surface, which is perpendicular to the silver nanoparticle surface.[28] The $\nu$(C–S) and $\nu$(S–S) bands cannot be detected because of the low-lying frequency of these bands and their relative weakness for infrared spectroscopy. Therefore, the chemical nature of the sulfur species cannot be determined. Nevertheless, IR suggests the presence of the peptide on the surface of the particle.

Figure 6 shows surface-enhanced Raman spectroscopy (SERS) data of P1. All SERS bands are relatively broad, which indicates that the peptides interact strongly with the surface. SERS detects two strong bands at 480 and 670 $cm^{-1}$. The former can be attributed to $\nu$(S–S) in the L-cystine di-

  

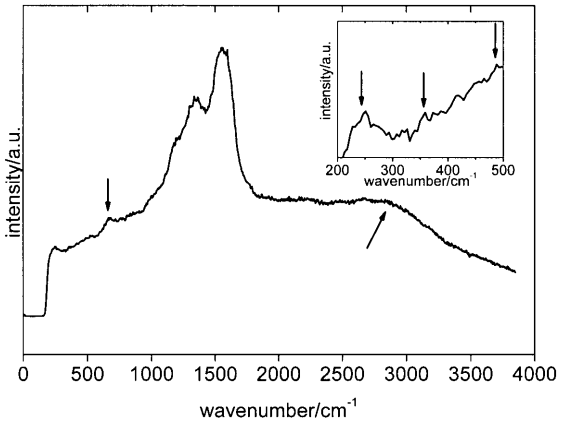


Figure 6. Surface-enhanced Raman spectrum of P1. Inset: Magnification of the 200 $cm^{-1}$–500 $cm^{-1}$ region. Arrows indicate bands described in the text.

sulfide and the latter to ν(C–S) in thiols.[65] SERS therefore shows that both the original dimeric peptide **4** (the disulfide) and the cleaved species (the thiol) are simultaneously present on the silver-particle surface. However, much like in our earlier study,[28] the weak signal at 240 $cm^{-1}$ is a superposition of ν(Ag–N)[66] and ν(Ag–S).[65] As a result, SERS cannot unambiguously identify the nature of the Ag–S bond on the metal surface.

The band at 356 $cm^{-1}$ can be attributed to a ν(Ag–O) band, which is indicative of a partially oxidized silver surface.[67] Peptide bands from 1169 to 1651 $cm^{-1}$ are indicative of a variety of structural orientations that are present at the surface. They can be attributed to $\delta$(C–H) and ν(N–H) of the peptide, similar to the assignments given for the deconvoluted IR spectrum in Figure 1.

There is no clear evidence of the $3_{10}$ structure because the amide I and amide II bands are superimposed with the $\nu$(N–H), and a clear interpretation of the amide bond orientation at the metal surface with this spectral resolution is not possible. However, the signal at around 2950 $cm^{-1}$ can be attributed to amide A vibrations and ν(C–H) present in the peptide. In summary, SERS measurements show that the peptide is connected to the nanoparticle surface and that both disulfide and thiol groups are bound to the silver surface. Moreover, SERS also shows that the silver is partially oxidized as we also detect a ν(Ag–O) band.

Figure 7 shows representative X-ray photoelectron spectroscopy (XPS) spectra of the particles. For all samples, the Ag $3d_{5/2}$ signals exhibit broad peaks with full widths at half maximum (FWHM) of around 1.3 eV by using the twin anode and 0.8 eV by using the monsource. The silver $3d_{5/2}$ and $3d_{3/2}$ are located at binding energies of 368.4 eV and 374.3 eV, respectively. These findings correlate with former studies of similar systems.[28,68] The broadened shape is due to the variety of conformations of the peptide on the particle, and a further contribution arises from the silver particle size.[68–71] This silver binding energy is representative of an oxidized metallic silver surface.[72–74] The high amount of

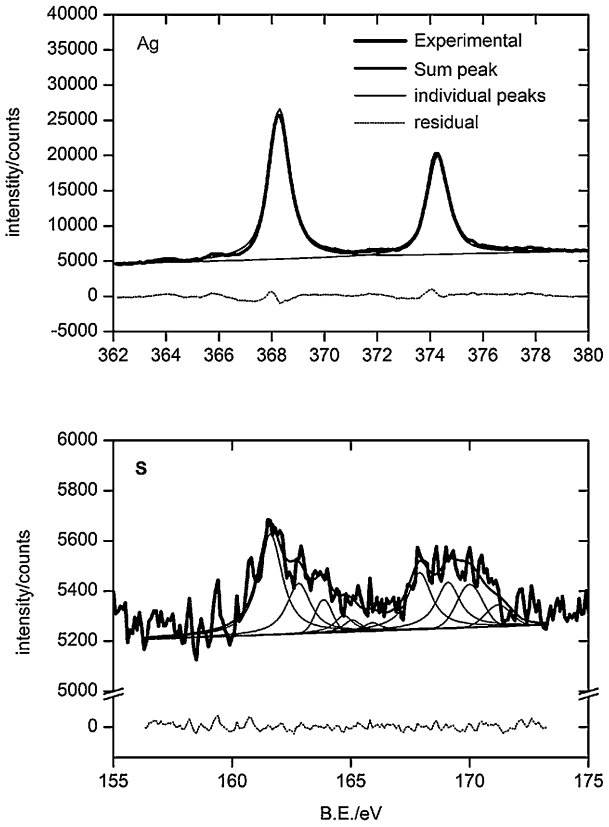


Figure 7. XPS spectra of the Ag and S edges of P2 (excitation source: $Mg_{K\alpha}$).

Table 3. Surface composition of P1 to P3 determined by using the monosource.[a]

| Signal | P1 | P2 | P3 |
|---|---|---|---|
| Ag $3d_{5/2}$ | 23.5 | 37.9 | 46.2 |
| C 1s | 61.7 | 42.6 | 31.0 |
| N 1s | 5.4 | 6.1 | 6.4 |
| O 1s | 9.4 | 13.4 | 16.4 |
| S 2p | (0.7) | (0.6) | (1.0) |

[a] The beam of the monosource has been directed on a rectangular powder rich surface area of 800 μm × 300 μm and therefore a contribution from the sample support (flexible graphite) is almost excluded. The sulfur content (in brackets) has been determined from measurements with the twin anode and is given with respect to all other species detected from an average surface area of 0.8 $cm^2$. All values are given in at %.

oxygen (see Table 3) at the silver nanoparticle surface indicates the presence of oxidized silver, as $Ag_2O$, and/or that some reducing agent is also adsorbed on the nanoparticle surface. Table 3 summarizes the surface composition of the three samples. It clearly shows that the metal/carbon ratio increases from P1 to P3.

Figure 8 shows that from P1 to P3, the amount of carbon species at higher binding energies increases. This indicates a change in the organic layer towards more-oxidized carbon species from P1 to P3. At the same time, the oxygen content increases from 9.4 to 16.4 at % and the oxygen to nitrogen ratio increases as well. XPS therefore suggests that particles prepared at pH 9 are partly still covered with ascorbate or

  

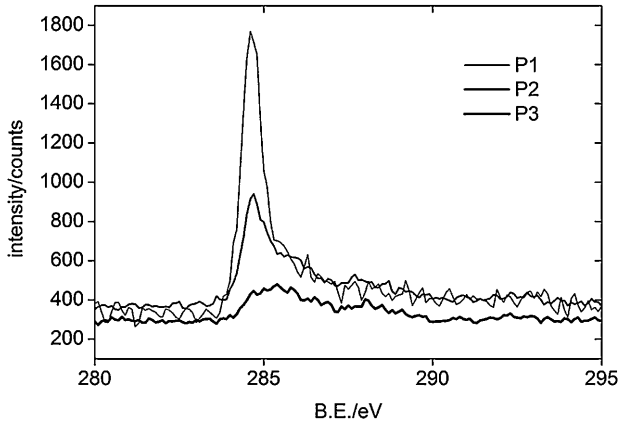


Figure 8. Energy evolution of the C 1s edge from P1 to P3 (excitation: monochromatic $Al_{K\alpha}$). B.E. = binding energy.

dehydroascorbate rather than with peptide. As a result, the P3 silver particles that were prepared are less efficiently capped by the peptide and expected to be less stable.

Table 4 shows that depending on the preparation pH, different signals are observed for sulfur S 2p in XPS. The signal

Table 4. Peak deconvolution of the S 2p peak.

| Sample | Bonding energy of sulfur S 2p peaks [eV] |
|---|---|
| P1 | 161.0; 161.7; 163.8; 167.7; 169.4 |
| P2 | 161.6; 163.9, 165.4, 167.95, 169.7 |
| P3 | 161.3; 162.0; 164.9; 167.0; 168.5; 170.5 |

at 161.7 eV is indicative of a thiol at the silver surface. Because of the high reactivity of thioethers and dithiols towards silver surfaces, the presence of a thiol is not surprising.[65,75] The signal at 163.9 eV is indicative of a cystine bridge chemisorbed on the silver surface. Higher energies are indicative of sulfoxide and cystine disulfoxide, probably from air exposure of the nanoparticles.[76] XPS spectra of P1 exhibit an additional signal at 161 eV caused by sulfide $S^{2-}$.[77] This may indicate a different mechanism of thiol cleavage, possibly through the direct cystine bridge reduction and cleavage of a C–S bond,[65,75] which is similar to one of our previous studies.[28]

Overall, XPS confirms SERS in the sense that we also detect a variety of chemical species including a mixture of disulfides and thiols on the silver surface and some oxidation of the particle surface. In addition, P1 shows a non-perfect disulfide bridge cleavage where presumably a significant fraction of the C–S bonds is broken. P2 particles do not show the signal corresponding to the $S^{2-}$ binding energy. They do, however, show about the same degree of silver oxidation (as shown by similar amount of oxygen on the surface) as P1. P3 exhibits high-energy sulfur peaks that suggest the presence of a large fraction of oxidized sulfur species. In summary, XPS clearly demonstrates the presence of peptide on the metal surface and also suggests that the peptide covers the particle more efficiently at neutral and acidic pH values rather than at basic pH values. Overall, the bond types (dithiol, thiol, sulfoxide, etc.) between the silver particle and the peptide are most uniform in sample P2. That is, in P2 we predominantly observe thiol molecules.

Figure 9 shows titration data for the peptide and P1 by using hydrochloric acid. The titration curve of the pure peptide is typical for molecules with two different, pH-responsive functional groups. The first equivalence point at a pH value of 5.1 corresponds to the deprotonation of the carboxylic acid groups at the C terminus of the peptide. The second equivalence point at a pH value of 8.5 is attributed to the deprotonation of the side chain ammonium groups. The titration curve of the nanoparticles only exhibits one equivalence point around pH 7. This can be explained by the fact that the titration was performed by using an excess of hydrochloric acid, that is, the peptide was back-titrated. As the concentration of peptide is low compared with the HCl, essentially only the titration of the excess HCl is visible. To obtain the same titration curve as for the pure peptide, the particle concentration would need to be 20.83 times larger. This corresponds to 4.17 g of modified SNP/40 mL of solution, which is not possible owing to solubility problems.

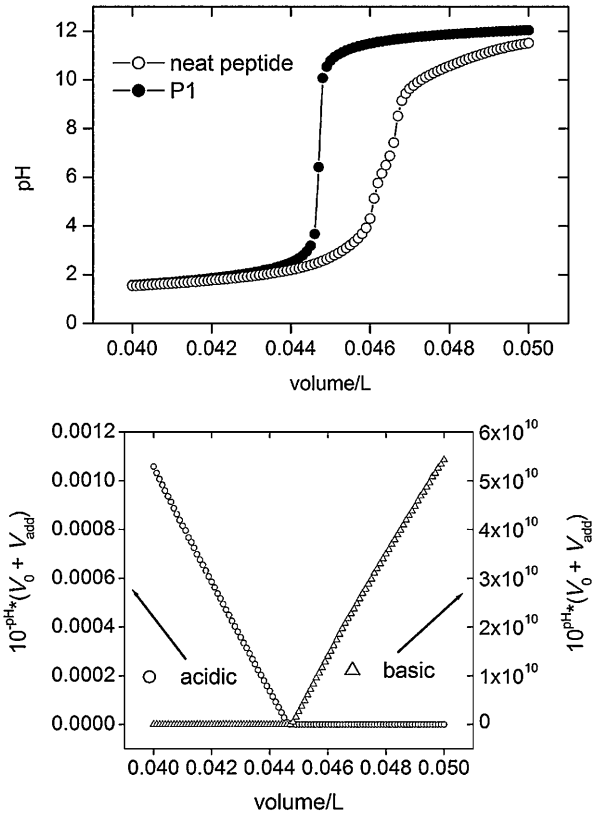


Figure 9. a) pH as a function of titrant added. b) Gran's treatment of titration data.[78]

Figure 9 also shows the results of Gran's analysis[78] that includes strong-acid, weak-acid or -base, and strong-base fractions. The difference between the strong-base and strong-acid fractions gives the amount of weakly acidic or

  

basic groups and allows determination of the concentration of peptide on the particle surface, which in the current case is 57.7 μmol $g^{-1}$. This corresponds to (on average) 1300 peptides per silver nanoparticle, assuming that the particle diameter of the silver core is 18.9 nm (average particle size, from TEM) and the volume of one silver nanoparticle is 94.4 $nm^3$ ($\rho_{Ag} = 10.59\ g\,cm^{-3}$). It is assumed that the peptide coverage is complete, that is, there is only peptide on the surface.

Figure 10 shows thermogravimetric analysis (TGA) data of P1 to P3. TGA curves show three distinct weight losses, 171 °C, 248 °C, and 370 °C. These can be assigned to the successive thermal destruction of the peptide layer on the particles. However, a precise mechanism of decomposition could not be formulated, as mass spectrometry data were not available. Above approximately 400 °C, silver reacts with oxygen, which causes the slight increase in mass observed in all cases at higher temperatures. P1 contains approximately 3.7 % of organic, P2 contains around 2.8 %, and P3 only contains approximately 1.4 %. In the case of P1, this represents around 1200 peptides per particle, which corresponds well with the findings from the titration experiments. TGA thus shows that the pH value of preparation has some influence on the amount of organic compound present on the surface. TGA is also consistent with titration data in which a maximum peptide fraction of 5 % for P1 was found. However, direct comparisons of P1 and P2 with P3 are not possible because of their difference in size.

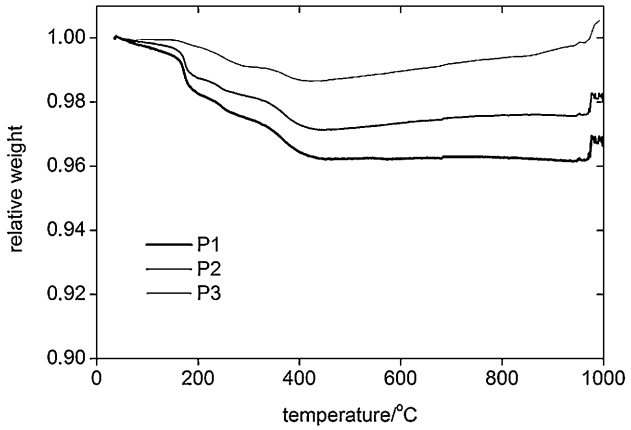


Figure 10. TGA curves of P1, P2, and P3.

**Responsive behavior and aggregation of peptide-modified silver particles**: Metal nanoparticle shapes and assembly in solution can easily be characterized by using UV/Vis spectroscopy.[79–81] Figure 11 shows typical UV/Vis spectra of P1, P2, and P3 in aqueous solutions of different pH. Figure 12 shows a representative example of a deconvoluted UV/Vis spectrum and Table 5 summarizes the deconvolution data for P1.

Figure 11 shows that all bands in the UV/Vis spectra are broad and often exhibit shoulders caused by overlapping bands. This indicates that 1) the particle-size distribution is broad and 2) that in some cases, not only spherical particles

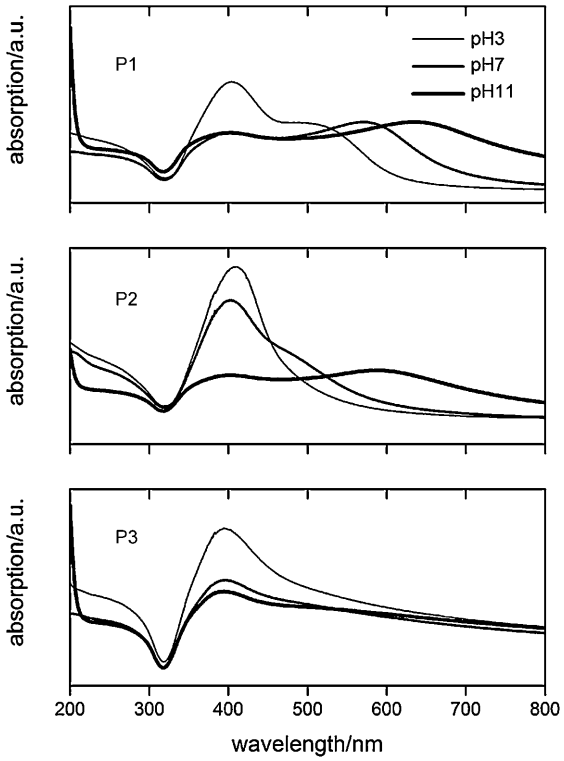


Figure 11. UV/Vis spectra of P1, P2, and P3 at different pH values. All spectra were recorded in solutions with a nanoparticle concentration of 0.2 mg $mL^{-1}$. The bands below 300 nm are from the peptide.

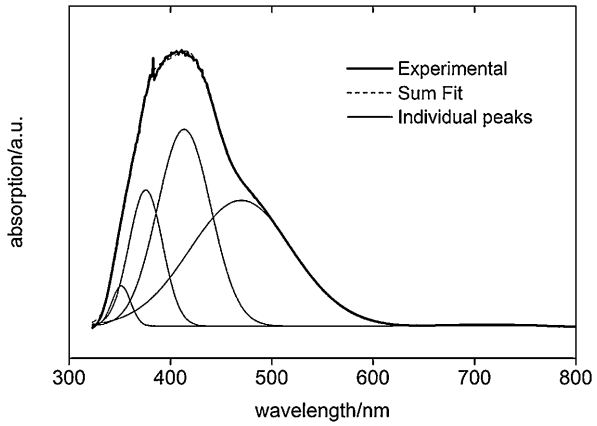


Figure 12. Representative deconvolution of a UV/Vis spectrum of P1 at pH 3. The sum fit overlaps with the experimental data and can only barely be seen at the top of the experimental peak at around 400 nm.

Table 5. UV/Vis spectral deconvolution of P1.[a]

| | Peak maximum [nm] |
|---|---|
| pH 9 | 347, 370, 405, 477, 625, 754 |
| pH 7 | 350, 372, 402, 463, 575, 696 |
| pH 3 | 351, 376, 414, 470 |

[a] Absorption bands were modeled by using Gaussian curves.

  

are present in the sample. Bands at around 350, 370, 400, and 470 nm have been assigned to scattering and plasmon resonance of single particles.[80,81] Bands around 500 nm have been assigned to bent or distorted particles,[80] bands at around 600 nm are due to triangular nanoparticles or to nanoparticle aggregates,[80] and bands at 700 nm and longer have been assigned to aggregates, raspberry-like shapes, or silver nanowires.[81] Only P3 shows a significant absorption at and above 700 nm, which is assigned to the various shapes observed in this particular sample (Figure 4).

Besides a preliminary shape assignment, UV spectroscopy provides a means to study particle aggregation in solution. P1 and P2 show a clear shift of the absorption maximum from approximately 400 nm to 700 and 750 nm, respectively, as the pH value changes from 3 to 11. As the particle shapes do not change, this is a clear indication of a stepwise aggregation. UV/Vis spectroscopy suggests that at each pH a specific type of aggregation occurs, as a different but broad absorption band is always detected. Furthermore, as the surface plasmon band of individual particles at 400 nm does not completely disappear, UV/Vis spectroscopy also suggests that in all cases some particles remain as isolated spheres. Moreover, the surface chemistry (and thus peptide loading) affects the shapes of the plasmon bands. For example, P1 at pH 7 is not equivalent to P2 at pH 7. However, on a qualitative level, the behavior is correlated in the sense that P1 and P2 (but not P3) follow the same trends. For simplicity, only the behavior of P1 particles, which have been shown to be the most uniform sample, will be discussed.

Figure 13 shows representative TEM images of samples taken at different pH. TEM confirms UV/Vis spectroscopy and shows that at pH 3, essentially all particles are present as isolated spheres and that virtually no aggregation occurs. At pH 7, smaller aggregates with 10 to 30 particles per aggregate are found, although there are also some isolated particles. At pH 11, virtually all particles have assembled into large structures and only very few isolated particles can be observed. Both TEM and UV/Vis spectra show that the process is reversible and that a lowering of the pH again leads to individual particles.

To more precisely describe the size of the aggregates and to rule out drying artifacts in the TEM images, the particles were analyzed by using dynamic light scattering (DLS). Although the analysis of the DLS data cannot be correlated directly to the TEM images owing to charge and absorption effects, especially at low pH in which the particles are highly charged, DLS provides evidence of aggregation that is consistent with TEM and UV/Vis spectra.

Table 6 shows the size of the aggregates versus the solution pH value. Clearly, an increase in the pH value leads to an increase in the hydrodynamic diameter $d_h$ of the aggregates. The transition between the different sizes (i.e. pH) is not abrupt. For example, at pH 6.5, there are at least two populations with significant intensity. This finding further supports the TEM observation of the presence of multiple types of aggregates; it also suggests a dynamic growth process.

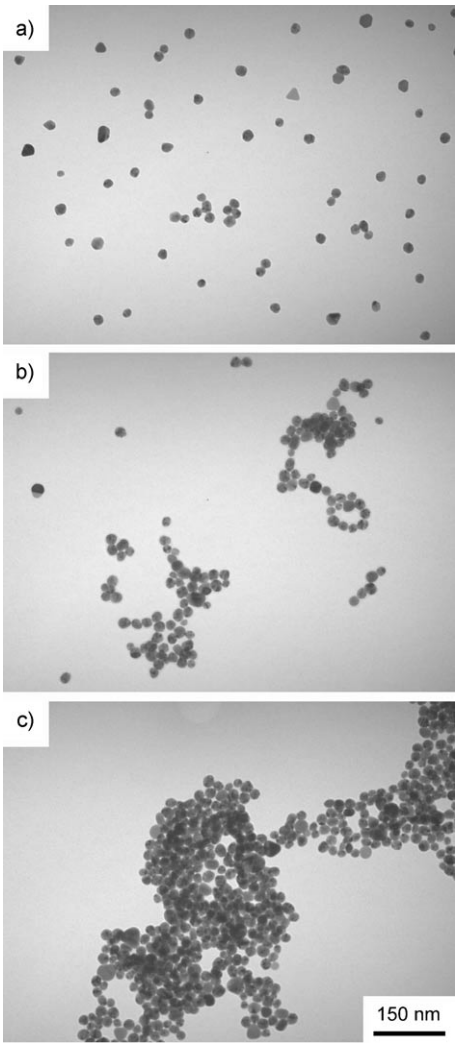


Figure 13. TEM images of P1 at a) pH 3, b) pH 7, and c) pH 11. Scale bar applies to all images.

Table 6. Aggregate dimensions extracted from DLS.[a]

| pH | $d_h$ | [%] | $d_h$ | [%] |
|---|---|---|---|---|
| 2.3 | 23.2 ± 13.0 | 100 | | |
| 6.3 | 22.5 ± 2.5 | 55 | 60.2 ± 14.4 | 45 |
| 7.3 | 60.8 ± 11.2 | 55 | 352.6 ± 83.5 | 45 |
| 8.4 | 684.0 ± 77.0 | 100 | | |
| 10.3 | 874.7 ± 108.3 | 100 | | |

[a] Volume weighted data are given, the hydrodynamic diameter $d_h$ is in nm

A simple calculation taking an average particle size of 18.9 nm (from TEM, Figure 4) indicates that at pH 2.3, the particles are present as monomers and possibly dimers, at pH 6.3 the particles are present as monomers (possibly dimers) and, predominantly, tetramers. At pH 10.3, the aggregates are mainly approximately 50-mers, but some very big aggregates (>300-mers) are also present. Larger aggregates may sediment; thus the size distribution at pH 10.3 is approximate. In summary, even with a simple analysis, DLS shows that aggregation takes place in solution, and this pro-

  

cess is pH dependent. DLS thus supports TEM and UV/Vis experiments (Figure 11 to Figure 13).

Small-angle X-ray scattering (SAXS) further supports DLS and provides both size-distribution quantification and an interaction-potential estimation. Figure 14 shows typical

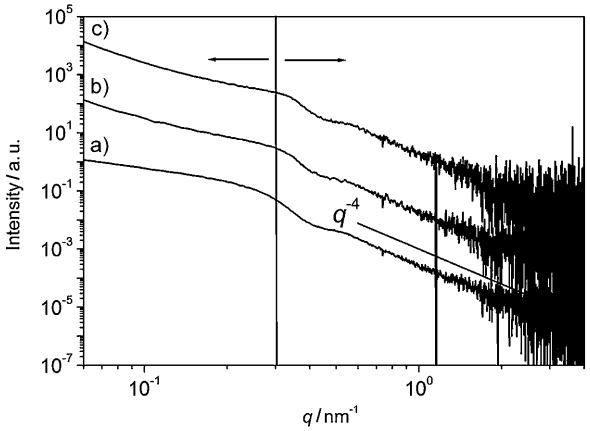


Figure 14. SAXS intensities of P1 at pH 2.28 (a), 6.30 (b), and 10.30 (c). Arrows indicate regions where interparticle interactions affect the scattering curves ($q<0.3\ nm^{-1}$) and where interactions can be neglected ($q>0.3\ nm^{-1}$). The Porod region ($I(q)\propto q^{-4}$) is indicated by a straight line. (b) and (c) are vertically shifted by a factor of $10^2$ and $10^4$, respectively, for clarity. SAXS data were obtained at a concentration of 1% (w/w) at a pH value between 2.3 to 10.3.

SAXS curves. The shape of all curves is identical at $q$ values larger than $0.3\ nm^{-1}$ that display a characteristic minimum around $0.4\ nm^{-1}$ and a Porod behavior ($I(q)\propto q^{-4}$) for $q>0.6\ nm^{-1}$. These characteristics indicate both a moderate polydispersity and a sharp interface between nanoparticles and their surroundings. A fractal particle surface can therefore be excluded and the peptide shell is practically invisible for SAXS. The increasing intensity and steepness of the SAXS curve in the lowest $q$ region shows that attractive interparticle interactions increase with increasing pH values. As a result, the form factor of P1 cannot be derived from a whole curve fitting by using a model function form factor, but the observation of increasing attraction with increasing pH is consistent with DLS and TEM (Figure 13 and Table 6).

The scattering intensities at high $q$ values ($0.3\ nm^{-1}<q<4\ nm^{-1}$) were used to determine the radius and polydispersity of the particles (Figure 15). In this range, particle interactions are negligible. The mean radius of P1 is $10.1\pm0.1$ nm and the polydispersity is $0.18\pm0.01$.These data are in good agreement with TEM and DLS (Figure 13 and Table 6).

Figure 15 also shows that there is a deviation between the experimental SAXS curve and the theoretical curve of noninteracting particles in the low $q$ region below $0.3\ nm^{-1}$. This deviation can be assigned particle–particle interaction effects. Quantitatively, the interaction is expressed in terms of the structure factor $S(q)=I(q)/P(q)$, where $I(q)$ is the intensity and $P(q)$ is the particle form factor (Figure 16).

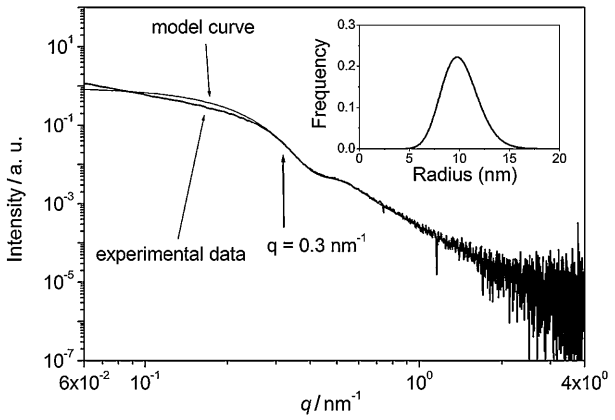


Figure 15. SAXS intensity of P1 at pH 2.28 and a model curve of polydisperse spheres with Schulz distribution fitted to the data beyond $q=0.3\ nm^{-1}$ (thick arrow). The inset displays the frequency of the radii of the Schulz distribution corresponding to the SAXS fit curve.

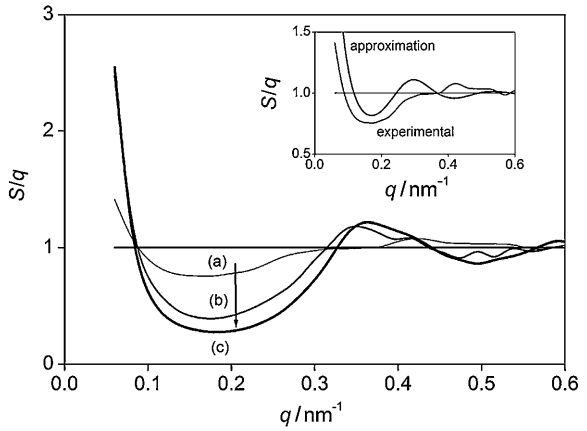


Figure 16. Structure factors of P1 at pH 2.28 (a), 6.30 (b), and 10.30 (c). Inset: Experimental structure factor at pH 2.28 (thin line) and approximation (thick line) with a square well potential with a depth of $U_0=5\ kT$ and a width of $\lambda=0.75$.

Experimental estimation of $S(q)$ by using a square well model (see the Experimental Section) resulted in interaction potentials of 5, 10, and 12 kT (12.3, 24.6, and 29.5 kJ mol$^{-1}$ at 293 K) for pH values of 2.28, 6.30, and 10.30, respectively. As a result, Figure 16 shows an increasing interparticle interaction with increasing pH values. This again confirms that the particle stickiness is pH dependent, although the assumption of a simple square well potential can certainly be optimized.

## Discussion

**Particle synthesis and peptide coating**: It has been pointed out previously that the formation of metal nanoparticles is strongly affected by the pH value of the solution.[13–15,25] It is also well known that thiols are efficient growth modifiers for metal nanoparticles.[82,83] In the current study, we have

  

used a peptide, which at the same time acts as a template for the formation of well-defined (P1 and P2) nanoparticles and also imparts pH-responsiveness to the silver particles. The effect on the particle growth is rather strong because both the cystine and the lysine moieties of our peptide can interact with $Ag^I$.[84] Therefore, the size and shape of the resulting particles are a result of the combined influence of the pH value and peptide chemistry.

TEM (Figure 3) shows that for the controlled formation of uniform particles, protonated lysine residues (P1 and P2, pH 3 and 7, respectively) are favorable. In this case, the lysine residues interact less strongly with the growing particle than if they are not protonated. The sulfur atoms provide the dominant interaction with the particle. The presence of negatively charged carboxylate groups and neutral amines (P3, pH 9) is less favorable, as large, irregularly shaped particles form (Figure 4). This is intriguing because intuitively, one would expect that with the combined adsorption of the disulfide and the free amine groups onto growing Ag particles there should be a more efficient interaction between the growing particle and the peptide and the particles should therefore be smaller. However, TEM and UV/Vis spectroscopy clearly show that positively charged ammonium groups on the lysine side chains are more favorable. We hypothesize that with too many adsorbing groups (four amine groups and one disulfide per peptide, 1200 to 1300 peptides per particle) there are too many competing interactions, which overall prevent an ordered particle growth.

TGA, titration, XPS, IR, and SERS show that the peptides are stably bound to the particle surfaces. XPS and SERS also show that 1) some of the peptide is present as a disulfide, 2) some is present as a thiol, and 3) that the peptides most likely form a brush on the particle surfaces. There is also evidence for Ag oxidation, which is similar to our earlier study.[28]

XRD suggests that the peptide is not, like regular thiols, simply sitting on the surface of the nanoparticles, but (at least on the dry particles) adopts a certain periodic order. This is clearly evidenced by the additional peak observed in the XRD patterns of the particles (Figure 3). Moreover, XRD shows that the peptide induces additional effects in the silver nanoparticles, as seen by the shifts of the (311) and (402) reflections (Table 2). Although the particle growth mechanism has not been investigated yet, XRD shows that the peptide acts as a simple and very mild capping agent, which is in contrast with the classically used thiols of the Brust–Schiffrin technique, which traps gold nanoparticles at early grow stages.[45,46] It is possible that the peptide used in the current study acts in a similar manner to a growth mechanism suggested by Naik et al.[41] These authors suggest that particles can grow by accumulation of silver atoms, which is mediated by the presence of oligopeptides. Typically, in these cases, the lowest energy faces are favored and particles with large (111) faces grow. Although this is not the case in the current study, we do observe a slight crystallographic anisotropy along (200) and (400) (Table 1). This suggests that both effects, the strong interaction of the disulfide and an accumulation of silver atoms in the vicinity of the peptide could contribute to the resulting particle sizes, shapes, and distortions. Further studies into this topic are, however, necessary to elucidate the growth mechanism and specific interactions of the peptide with the growing particles in more detail.

XRD (Table 1) also shows the effect of the peptide on the crystal structure of the silver particles. Similar to a few earlier studies[62,63,85–87] in which small molecules were investigated, the current study reveals that also peptides influence the crystallographic structure of the SNPs in a specific fashion.

**Reversible particle aggregation**: TEM, DLS, and UV/Vis spectroscopy (Figures 11–13, Table 5, and Table 6) show that the aggregation of the peptide-modified nanoparticles can be controlled by variation of the pH value and that particle aggregates with discrete sizes (although a broad size distribution) form as a function of the solution pH value. At pH 3, the lysine side chains and the C-terminal carboxylic acid groups (Scheme 1) are protonated, which leads to a positively charged shell. As a result of the high positive charge, particles exist as individual species and no aggregation occurs. At pH 7, the C-terminal carboxylic acid is deprotonated and the lysine residues are still protonated. Owing to the resulting zwitterionic particle surface, some aggregation occurs and small clusters of particles are observed in the TEM (Figure 13, Table 6).

At pH 11, the C-terminal carboxylate (Scheme 1) is deprotonated and carries a negative charge, but the lysine residues are not charged anymore. At this pH value, the particles assemble into large aggregates. Presumably, the repulsive forces exerted by the single terminal carboxylate groups are not sufficient to prevent aggregation. Furthermore, as the deprotonated lysine is less hydrophilic, hydrophobic interactions and hydrogen bonding can occur, leading to the large aggregates.

SAXS qualitatively supports TEM, DLS, and UV/Vis spectroscopy in that an approximate interaction potential can be estimated, which increases with increasing pH value. Because the interaction potential is attractive at all pH values, it supports the observation that the particles can form small, weakly bound aggregates, which reversibly form and disassemble with variation of the pH value.

**Potential of the peptide-functionalized particles**: The aggregation process is reversible and can easily be controlled by the pH value. Furthermore, the particles contain further (chiral) information that is not lost in the solid state (XRD, Figure 3). Our approach therefore enables the preparation of silver nano-objects that can be viewed as building blocks for biomimetic or bioinspired hybrid materials, which can be reversibly assembled and disassembled. They are therefore interesting for materials where, for example, the optical properties need to change upon an external stimulus or where a response upon a change in a biological environment is desired.

  

Our model system is just one example of a stimulus-responsive material. Modification of the peptide sequence and the metal core will lead to a wide variety of other particles. For example, one can envision materials that are composed of two or more components, such as peptide-coated gold and silver particles. The resulting materials should have interesting optical properties, in particular, because the peptide coating provides additional chiral information.

On the experimental side, disulfides are convenient because they avoid the additional steps of thiol protection and deprotection without losing efficiency in the peptide attachment. This work therefore extends our previous study in which it has been shown that thioether- (and not disulfide) bearing peptides are efficient growth modifiers for SNPs.[28]

A further advantage of our current approach is that a ligand-exchange reaction (which are not always effective) is not used,[52,88,89] but rather a mild reduction process for particle synthesis. The approach is simpler than the approach by Levy et al.,[52] and the results are similar to data by Si, Mandal and co-workers with a water-soluble peptide,[42,43] but are very different from Xie et al.,[90] who prepared plate-like particles.

## Conclusion

Herein, we show that peptides based on a disulfide bridge can be efficiently used for the synthesis of peptide-coated nanoparticles. At low pH values, individual particles are present. At high pH values, large aggregates form. These can be disintegrated again by lowering the pH value. There is also evidence for the formation of different aggregate sizes, depending on the pH value. The main asset of the current system is its synthetic simplicity, with two identical tripeptides connected by a disulfide bond. The disulfide simplifies the synthesis while maintaining full responsiveness of the peptide in aqueous solution. To our best knowledge, this is the first study of a stimulus-responsive silver nanoparticle/peptide hybrid material in an aqueous environment. Somewhat simpler than an earlier gold-nanoparticle-based system, it nevertheless keeps its responsiveness.[52]

In summary, we present a simple, yet flexible system for the synthesis of complex materials. The most intriguing feature is probably the fact that the structure of the nanoparticle aggregates depends only on the solution pH value, but in a very interesting way: instead of a simple precipitation—dissolution, variation of the pH value leads to individual nanoparticles, small, or large aggregates. Overall, our study suggests that metal nanoparticle/peptide hybrid materials could be interesting for applications in which a reversible response to an external stimulus (in this case, pH value) is desired, such as medicine, biotechnology, or optical devices.

## Experimental Section

**Peptide synthesis**: Amino acids were purchased from Bachem AG (Bubendorf, Switzerland) and chemicals from Fluka (Buchs, Switzerland). All chemicals were used as received. All amino acids are L-amino acids. Chemical shifts are shown in ppm compared with TMS.

**Synthesis of Z-Lys(Boc)-Lys(Boc)-O*t*Bu (1)**: To an ice-cooled solution of Z-Lys(Boc)-OH (7.3 g, 19.2 mmol, 1.3 equiv; Boc = *tert*-butoxycarbonyl) in chloroform (70 mL), 4-methylmorpholine (2.43 mL, 22.15 mmol, 1.5 equiv) was added and the solution was stirred under Ar for 5 min. Then, isobutyl chloroformate (2.7 mL, 20.7 mmol, 1.4 equiv) were added and the solution was stirred for 2 min. To this solution, H-Lys(Boc)-O*t*Bu HCl salt (5 g, 14.75 mmol, 1 equiv) was added, followed by careful addition of 4-methylmorpholine (1.62 mL, 14.75 mmol, 1 equiv). After 15 min, the cooling was removed and the solution was allowed to warm up to room temperature and stirred overnight. Then, chloroform (200 mL) was added and the solution was washed with sodium hydrogenocarbonate solution (3×100 mL), saturated brine (100 mL), 10% citric acid solution (3×100 mL), saturated brine (100 mL), and deionized water (2×100 mL). The organic phase was dried over sodium sulfate and evaporated to dryness. The solid **1** was crystallized from chloroform/diethyl ether and dried in a vacuum oven at 40 °C, yielding a white powder (4.3 g, 49%). $^1$H NMR (400 MHz, [D$_6$]DMSO): $\delta$ = 8.05 (m, 0.82 H, H$_{amide}$), 7.31 (m, 5.5 H, H$_{phenyl}$ + 1 H$_{phenyl\ carbamate}$), 6.73 (m, 1.73 H, 1.73× H$_{\textit{tert}\text{-butyl carbamate}}$), 6.38 (m, 0.15 H, 0.15× H$_{\textit{tert}\text{-butyl carbamate}}$), 4.99 (m, 2.04 H, H$_{phenyl}$), 4.00 (m, 1.86 H, H$_{\alpha\text{-Lysine 1}}$ + H$_{\alpha\text{-Lysine 2}}$), 2.90 (m, 3.95 H, H$_{\beta\text{-Lysine 1}}$ + H$_{\beta\text{-Lysine 2}}$), 1.50 (m, 4.25 H, H$_{\gamma\text{-Lysine 1}}$ + H$_{\gamma\text{-Lysine 2}}$), 1.30 ppm (m, 35 H, H$_{\textit{t}\text{-butyl ester}}$ + H$_{\text{Boc Lysine 1}}$ + H$_{\text{Boc Lysine 2}}$ + H$_{\delta\text{-Lysine 1}}$ + H$_{\delta\text{-Lysine 2}}$ + H$_{\varepsilon\text{-Lysine 1}}$ + H$_{\varepsilon\text{-Lysine 2}}$). N 8.37; $^{13}$C NMR (100 MHz, [D$_6$]DMSO): $\delta$ = 172.95, 172.02, 156.77, 156.41, 137.91, 129.17, 128.61, 128.55, 81.22, 78.17, 66.18, 55.19, 53.50 , 32.57, 31.54, 30.10, 29.93, 29.13, 28.46, 23.71, 23.46 ppm; ATR-IR (neat): $\tilde{\nu}$ = 3334, 2973, 2932, 2867, 1688, 1514, 1452, 1244, 1159, 1043, 853, 777, 739, 695, 617 cm$^{-1}$; FAB-MS: *m*/*z*: calcd for $[M-H]^+$ = 665; measured $[M-H]^+$ = 665; elemental analysis calcd (%): C 61.42, H 8.49, N 8.43, O 21.66; found: C 61.35, H 8.25.

**Synthesis of NH$_2$-Lys(Boc)-Lys(Boc)-O*t*Bu (2)**: Compound **1** (4.3 g, 6.47 mmol, 1 equiv) was dissolved in methanol (50 mL) and the solution with degassed with argon. To this solution, Pd/C catalyst (108 mg) was added. The solution was hydrogenated at room temperature and at 50 bar overnight. The resulting black solution was filtered over sea sand and the sea sand was carefully washed with portions of methanol. The remaining catalyst was removed by centrifugation, the solvents were evaporated to dryness and the residue was left overnight in a vacuum oven at 40 °C to yield **2** (3.25 g; 95%). $^1$H NMR (400 MHz, [D$_6$]DMSO,): $\delta$ = 8.4 (m, 0.1 H, H$_{amide}$), 8.03 (m, 0.9 H, H$_{amide}$), 6.74 (m, 1.86 H, H$_{Boc}$ + H$_{Boc}$), 6.37 (m, 0.14 H, H$_{Boc}$ + H$_{Boc}$), 4.06 (m, 1 H, H$_{\alpha\text{-Lysine 1}}$), 3.12 (m, 1 H, H$_{\alpha\text{-Lysine 2}}$), 2.87 (m, 4 H, H$_{\varepsilon\text{-Lysine 1+2}}$), 1.63 (m, 1.42 H, H$_{\beta\text{-Lysine 1}}$), 1.53 (m, 2.51 H, H$_{\beta\text{-Lysine 1}}$ + H$_{\beta\text{-Lysine 2}}$), 1.3 ppm (m, 35 H, H$_{\text{Boc Lysine 1}}$ + H$_{\text{Boc Lysine 2}}$ + H$_{\textit{t}\text{-butyl ester}}$ + H$_{\gamma\text{Lysine 1}}$ + H$_{\gamma\text{-Lysine 2}}$); $^{13}$C NMR (100 MHz, [D$_6$]DMSO,): $\delta$ = 175.89, 172.16, 156.42, 156.40, 81.37, 78.17, 78.15, 55.04, 53.08, 49.45, 35.61, 31.89, 30.30, 29.94, 29.13, 28.48, 23.39, 23.37, 23.36 ppm; ATR-IR (neat): $\tilde{\nu}$ = 3358, 2975, 2938, 2867, 1720, 1686, 1655, 1519, 1502, 1457, 1392, 1365, 1338, 1252, 1160, 1061, 1037, 996, 867, 846, 778, 747, 696, 617 cm$^{-1}$; FAB-MS: *m*/*z*: calculated for $[M-H]^+$ = 531; measured $[M-H]^+$ = 531; elemental analysis calcd (%): C 58.84, H 9.50, N 10.56, O 21.10; found: C 57.67, H 9.20, N 10.45.

**Synthesis of (Boc-Cys-Lys(Boc)-Lys(Boc)-O*t*Bu)$_2$ (3)**: (Boc-Cys-OH)$_2$ (cystine bridge) (1 g, 2.55 mmol, 0.9 equiv) was dissolved in THF (9 mL) under argon, and the resulting solution was cooled with an ice bath. 4-Methylmorpholine (2.7 mL, 12.3 mmol, 4.4 equiv) was added to this solution and the solution was stirred for 5 min. Then, isobutyl chloroformate (1.5 mL, 12.3 mmol, 2.2 equiv) were added and the slurry was stirred for 13 min. To this solution, **2** (3 g, 5.6 mmol, 1 equiv) dissolved in DMF (40 mL) was carefully added, and the mixture was stirred for 30 min with ice cooling. Then, the ice bath was removed and the slurry stirred for 48 h. Chloroform (200 mL) was then added and the solution was washed with sodium hydrogen carbonate solution (3×100 mL), saturated brine (100 mL), 10% citric acid solution (3×100 mL), saturated brine

  

(100 mL), and deionized water (2×100 mL). The organic phase was dried over sodium sulfate and evaporated to dryness. The solid **3** was crystallized from chloroform/pentane as a white powder and was dried in a vacuum oven at 40 °C (2.7 g, 65 %). $^1$H NMR (400 MHz, [D$_6$]DMSO): $\delta$ = 8.30 (0.23 H, m, H$_{amide}$), 8.16 (1.23 H, m, H$_{amide}$), 8.00 (0.71 H, m, H$_{amide}$), 7.80 (0.91 H, m, H), 7.12 (1.4 H, m, H$_{Boc}$), 6.72 (4.0 H, H$_{Boc}$), 6.30 (0.4 H, m, H), 4.28 (1.65 H, m, H$_{\alpha\text{-Lysine 1}}$), 4.15 (0.9 H, m, H$_{\alpha\text{-Lysine 2}}$), 4.00 (3 H, m, H$_{\alpha\text{-Lysine 3}}$ + H$_{\alpha\text{-Lysine 4}}$ + H$_{\alpha\text{-Cystine 2}}$), 3.69 (1.28 H, m, H$_{\beta\ \text{Cystine 1}}$), 3.30 (0.62 H, m, H$_{\beta\ \text{Cystine 2}}$), 3.20 (0.26 H, m, H$_{\beta\text{-Cystine 1}}$), 3.06 (1.48 H, m, H$_{\beta\text{-Cystine 1}}$ + H$_{\beta\text{-Cystine 2}}$), 2.84 (9.8 H, m, H$_{\beta\text{-Lysine}}$), 1.60 (4 H, m, H$_{\gamma\text{-Lysine 1}}$ + H$_{\gamma\text{-Lysine 2}}$), 1.51 (5.3 H, m, H$_{\gamma\text{-Lysine 3}}$ + H$_{\gamma\text{-Lysine 4}}$) , 1.33 (71 H, m, H$_{Boc\times 6}$ + H$_{\varepsilon\text{-Lysine 1}}$ + H$_{\varepsilon\text{-Lysine 2}}$ + H$_{\varepsilon\text{-Lysine 3}}$ + H$_{\varepsilon\text{-Lysine 4}}$ + H$_{\delta\text{-Lysine 1}}$), 0.8 ppm (6 H, m, H$_{\delta\text{-Lysine 1}}$ + H$_{\delta\text{-Lysine 2}}$ + H$_{\delta\text{-Lysine 3}}$); MALDI-TOF: *m*/*z*: calculated [*M*−H]$^+$ = 1465, measured [*M*−H]$^+$ = 1465; elemental analysis calcd (%): C 55.72, H 8.53, N 9.59, O 21.83, S 4.37; found: C 55.61, H 8.38, N 9.36.

**Synthesis of (TFA.NH$_2$-Cys-Lys(NH$_2$TFA)-Lys(NH$_2$TFA)-OH)$_2$ (4)**: Iced cooled 95 % TFA/water (v/v) solution (20 mL) was added to peptide **3** (2.7 g). The solution was stirred for 2 h. Solvents and reagents were removed under vacuum and the residual solvents were azeotropically removed by using chloroform (3×100 mL). The resulting, slightly yellow solid peptide **4** was dried overnight in a vacuum oven at 40 °C (2.63 g, 99 %). $^1$H NMR (400 MHz, [D$_6$]DMSO): $\delta$ = 8.8 (m, 1.0 H, H$_{amide}$), 8.5 (m, 3 H, H$_{amide}$), 8.25 (m, 0.5 H, H$_{amide}$), 8.12 (m, 0.5 H, H$_{amide}$), 8.08 (m, 0.75 H, H$_{amide}$), 7.9 ppm (m, 8 H, 2 H$_{\text{lysine carboxylic acid}}$ + 6 H$_{\text{TFA carboxylic acid}}$), 4.34 (m, 1.4 H, H$_{\alpha\text{-Lysine 1}}$), 4.13 (m, 3.24 H, H$_{\alpha\text{-Lysine 2}}$ + H$_{\alpha\text{-Lysine 3}}$ + H$_{\alpha\text{-Lysine 4}}$), 3.9 (m, 1.18 H, H$_{\beta1\text{-Cystine 1}}$), 3.7 (m, 1.37 H, H$_{\beta1\text{-Cystine 2}}$), 2.9 (m, 1.4 H, m, 1.18 H, H$_{\beta2\text{-Cystine 1}}$), 2.7 (m, 8.5 H, H$_{\beta\text{-Lysine 1}}$ + H$_{\beta\text{-Lysine 2}}$ + H$_{\beta\text{-Lysine 3}}$ + H$_{\beta\text{-Lysine 4}}$), 1.9 (m, 1.34 H, H$_{\beta2\text{-Cystine 1}}$), 1.74 (m, 3.74 H, H$_{\beta2\text{-Cystine 2}}$), 1.50 (m, 4 H, H$_{\varepsilon\text{-Lysine 1}}$ + H$_{\varepsilon\text{-Lysine 2}}$), 1.30 (m, 6 H, H$_{\varepsilon\text{-Lysine 4}}$ + H$_{\varepsilon\text{-Lysine 3}}$ + H$_{\delta\text{-Lysine 1}}$) 0.8 ppm (m, 6 H, H$_{\delta\text{-Lysine 2}}$ + H$_{\delta\text{-Lysine 3}}$ + H$_{\delta\text{-Lysine 4}}$); $^{13}$C NMR (100 MHz, [D$_6$]DMSO): $\delta$ = 174.28, 174.20, 174.14, 172.98, 171.91, 167.64, 167.46, 167.24, 160.00, 159.67, 159.35, 159.01, 157.07, 119.00, 116.12, 70.70, 55.00, 53.82, 52.82, 52.50, 52.38, 51.90, 32.48, 32.10, 31.10, 28.48, 28.41, 27.53, 27.47, 27.37, 23.29, 23.23, 23.18, 23.14, 22.90 ppm; ATR-IR (neat): $\tilde{\nu}$ = 3269, 3061, 3942, 2877, 2652, 2542, 2877, 2652, 2542, 1659, 1635, 1525, 1474, 1430, 1392, 1331, 1181, 1126, 836, 795, 716 cm$^{-1}$. MALDI-TOF: *m*/*z*: calcd for [*M*−H]$^+$ = 753, found [*M*−H]$^+$ = 753; calcd [*M*−Na]$^+$ = 775, found 775; elemental analysis calcd (%): C 35.10, H 4.63, N 9.75, O 22.75, S 4.46, F 23.80; found: C 35.78, H 4.93, N 8.69.

**Nanoparticle synthesis**: To 0.2 M silver(I) nitrate solution (5 mL, 1 mmol), a pH X (X = 3, 7, 9) solution of peptide **4** (0.059 mmol, 5 mL) was added. The mixture was stirred for 12 h in the dark. Then 1.5 M aqueous sodium ascorbate solution (2 mL, 3 mmol) and an aqueous solution of the peptide **4** (5 mL, 0.059 mmol) at pH 3 were added. The mixture was stirred for 12 h in the dark. The nanoparticles were purified during for sequences of centrifugation (14000 rpm, 3 mL Teflon centrifugation tubes) and washing with ultrapure water befor lyophilization. Sample 1 (denoted P1) was prepared at pH 3, sample 2 (P2) at pH 7, and sample 3 (P3) at pH 9. TGA shows a capping of the nanoparticles with the peptide of around 5 % for P1 and P2, and a capping of 2 % for P3.

**Thermogravimetric analysis**: TGA was performed with a Mettler Toledo TGA/SDTA 851e from 25 to 1000 °C with a heating rate of 10 °C.min$^{-1}$ in $N_2$.

**Potentiometry**: Potentiometric titrations were performed on a Mettler Toledo T 50 automatic titrator with a DG-115 SC glass electrode at 25 °C. Silver nanoparticles (197.7 mg) were suspended in a mixture of 0.03 M hydrochloric acid and 0.5 M sodium chloride solution (40 mL). During titration, 0.25 M sodium hydroxide (10 mL) was delivered in aliquots of 0.1 mL from the titrator. The time interval between additions was 90 s. Prior to titration, the electrode was calibrated by titrating a mixture of 0.1 M ammonia acetate and 0.1 M hydrochloric acid with 0.5 M sodium hydroxide. Data were analyzed by using Microsoft Office 2003 Excel software employing Gran's method.[78]

**X-ray diffraction (XRD) and Rietveld refinement**: XRD was done on a Nonius PDS 120 with a position sensitive detector (1 to 120° 2$\theta$ by using Cu$_{K\alpha}$ radiation. Rietveld refinement was performed by using Fullprof version 4.00 (May 2008).[64] The peaks were fitted with a Thompson–Cox–Hastings pseudo-Voigt profile that was convoluted with an axial divergence asymmetry function.[91] The instrumental resolution function was determined according to Louër.[92] Anisotropic strain broadening was used as implemented,[93] but the anisotropic size broadening was modeled by using the Scherrer formula written as a linear combination of spherical harmonics.[94] GFourier[64] was used to generate average crystallite shapes.

**X-Ray photoelectron spectroscopy (XPS)**: XPS measurements have been performed by using a VG ESCA Lab 220iXL (Thermo VG Scientific) spectrometer equipped with a twin anode (Mg$_{K\alpha}$ and Al$_{K\alpha}$ line) and an X-ray source providing monochromatic Al$_{K\alpha}$ light for excitation of the photoelectrons. The take-off angle was 90° to the surface and the pressure during the measurements was approximately $10^{-10}$ mbar. Silver nanoparticles were deposited on a roughened flexible graphite surface to avoid charging effects. For the quantification of the detected elements the X-ray spot of the monosource, which is 500 μm$^2$ in size, was directed on powder rich regions of the sample. To obtain S 2p signals with reasonable intensity for quantification and interpretation of the binding state of the sulfur, the twin anode (Mg$_{K\alpha}$ (1253.6 eV)) was used. In this case, the complete surface of the sample was excited and the analyzed area was defined by the settings of the analyzer which was 0.8 cm$^2$.

**NMR, IR, and UV/Vis spectroscopy**: $^1$H and $^{13}$C NMR spectra were recorded on an Avance 400 MHz NMR spectrometer. Infrared spectra were obtained from the neat samples on a Shimadzu FTIR 8300 with a Golden Gate ATR unit. Spectra were recorded from 300 cm$^{-1}$ to 4000 cm$^{-1}$ with a resolution of 1 cm$^{-1}$. FAB-MS spectra were taken on a Finnigan MAT 312. MALDI-TOF spectra were recorded on a Voyager-DE Pro (Applied Bioscience) by using α-cyano-hydroxycinnamic acid as the matrix. UV/Vis spectroscopy was performed in a quartz cuvette with an optical path length of 1 cm on a Perkin Elmer Lambda. Data were deconvolution was performed by using Fityk.

**Transmission electron microscopy (TEM)**: TEM images were taken by using an FEI Morgani 268D operated at 80 kV. Samples were deposited on carbon-coated copper grids and directly imaged after drying in air. Some samples were diluted prior to imaging to allow for better imaging conditions. Particle sizes were determined by measuring over 500 particles per sample from several images.

**Surface-enhanced Raman spectroscopy (SERS)**: Silver nanoparticles were investigated as neat powders with a confocal Raman microscope (CRM300, WITec, Germany) equipped with a piezo-scanner (P-500, Physik Instrumente, Germany), a 60× objective, and a 532 nm Nd:YAG laser. The spectra were acquired by using an air-cooled CCD detector (DU401-BV, Andor, UK) with 600 gratings/mm (UHTS 300, WITec, Germany). ScanCtrlSpectroscopyPlus (version 1.38, WITec) was used for data acquisition and processing.

**Dynamic light scattering (DLS)**: DLS experiments were performed on a Zetasizer ZS (Malvern Instruments, UK) on particle dispersions in distilled water in a disposable plastic cuvette. Experiments were performed at 20±1 °C. Samples were not filtered before measurements. The laser wavelength was 633 nm and data were recorded in backscattering mode at 2$\theta$ = 173°. At least ten 10 s measurements were made and data were averaged. A regularized inverse Laplace transformation based on the Contin algorithm as implemented in the Malvern Software DTS 5.02 was used for data analysis. The concentration was adjusted to avoid strong particle–particle repulsion through electrostatic interactions and to account for an optimum count rate (around 200 kcps). Optical properties of bulk metallic silver[95] ($n$ = 0.56 and $k$ = 4.27 at 633 nm, where $n$ is the real part and $k$ is the imaginary component of the silver refractive index) were used for data analysis.

**Small-angle X-ray scattering (SAXS)**: SAXS measurements were performed with a Kratky-type instrument (SAXSess from Anton Paar, Austria). The SAXSess has a low sample-to-detector distance which is suitable for investigation of low scattering intensities. The measured intensity was corrected by subtracting the intensity from a capillary filled with pure water. The scattering vector is defined in terms of the scattering angle $\theta$ and the wavelength $\lambda$ of the radiation ($\lambda$ = 0.154 nm): thus $q = 4\pi/\lambda \sin(\theta/2)$. Deconvolution (desmearing) of the SAXS curves was performed with the SAXS-Quant software (version 2.0) from Anton Paar.

  

An analytic solution for Schulz-type polydisperse spheres[96] was used for determination of mean particle radius of $\langle R\rangle$ and polydispersity of $\sigma/\langle R\rangle$. *S(q)* was modeled with a square well potential.[97] The square well potential *U(r)* is identical to the hard sphere interaction for distances shorter than the particle radius, that is, $U(r)=\infty$ (hard sphere interaction), $-U_0$ for distances $\langle R\rangle < r < \lambda\langle R\rangle$ (attractive) and zero for $r > \lambda\langle R\rangle$.

## Acknowledgements

We thank Prof. E. C. Constable for access to his IR spectrometer, Prof. B. Giese for access to his MALDI-TOF apparatus, and D. De Bruyn for the MALDI-TOF measurement. A. Mantion thanks the Adolf-Martens-Fonds e.V. for an Adolf Martens Fellowship. a. Masic is grateful for support by the Alexander von Humboldt Foundation and the Max Planck Society in the framework of the Max Planck Research Award by the Federal Ministry of Education and Research. The Swiss National Science Foundation, the University of Potsdam, the Federal Institute for Materials Research and Testing, and the Max-Planck-Institute of Colloids and Interfaces are acknowledged for financial support.

[1] D. D. Evanoff, G. Chumanov, *ChemPhysChem* **2005**, *6*, 1221–1231.
[2] K.-S. Lee, M. A. El-Sayed, *J. Phys. Chem. B* **2006**, *110*, 19220–19225.
[3] M. Kang, R. Jung, H.-S. Kim, J. H. Youk, H.-J. Jin, *J. Nanosci. Nanotechnol.* **2007**, *7*, 3888–3891.
[4] A. Panacek, L. Kvítek, R. Prucek, M. Kolar, R. Vecerova, N. Pizúrova, V. K. Sharma, T. Nevecna, R. Zboril, *J. Phys. Chem. B* **2006**, *110*, 16248–16253.
[5] M.-C. Daniel, D. Astruc, *Chem. Rev.* **2004**, *104*, 293–346.
[6] A. Henglein, *Chem. Rev.* **1989**, *89*, 1861–1873.
[7] P. Chen, L. Song, Y. Liu, Y.-e. Fang, *Radiat. Phys. Chem.* **2007**, *76*, 1165–1168.
[8] Y.-O. Kang, S.-H. Choi, A. Gopalan, K.-P. Lee, H.-D. Kang, Y. S. Song, *J. Non-Cryst. Solids* **2006**, *352*, 463–468.
[9] F.-K. Liu, Y.-C. Hsu, M.-H. Tsai, T.-C. Chu, *Mater. Lett.* **2007**, *61*, 2402–2405.
[10] S. Remita, P. Fontaine, E. Lacaze, Y. Borensztein, H. Sellame, R. Farha, C. Rochas, M. Goldmann, *Nucl. Instrum. Methods Phys. Res. Sect. B* **2007**, *263*, 436–440.
[11] A. Taubert, I. Arbell, A. Mecke, P. Graf, *Gold Bull.* **2006**, *39*, 205–211.
[12] I. Pastoriza-Santos, L. M. Liz-Marzan, *Pure Appl. Chem.* **2000**, *72*, 83–90.
[13] S. P. Mushran, M. C. Agrawal, R. M. Mehrotra, R. Sanehi, *J. Chem. Soc. Dalton Trans.* **1974**, 1460–1462.
[14] I. Sondi, D. V. Goia, E. Matijevic, *J. Colloid Interface Sci.* **2003**, *260*, 75–81.
[15] L. Suber, I. Sondi, E. Matijevic, D. V. Goia, *J. Colloid Interface Sci.* **2005**, *288*, 489–495.
[16] P. C. Lee, D. Meisel, *J. Phys. Chem.* **1982**, *86*, 3391–3395.
[17] V. Privman, D. V. Goia, J. Park, E. Matijevic, *J. Colloid Interface Sci.* **1999**, *213*, 36–45.
[18] J. Turkevich, P. C. Stevenson, J. Hillier, *J. Phys. Chem.* **1953**, *57*, 670–673.
[19] J. Turkevich, P. C. Stevenson, J. Hillier, *Discuss. Faraday Soc.* **1951**, *11*, 55–75.
[20] J. A. Dahl, B. L. S. Maddux, J. E. Hutchison, *Chem. Rev.* **2007**, *107*, 2228–2269.
[21] H. Chih-Ching, Y. Zusing, C. Huan-Tsung, *Langmuir* **2004**, *20*, 6089–6092.
[22] Y.-F. Huang, Y.-W. Lin, H.-T. Chang, *Nanotechnology* **2006**, *17*, 4885–4894.
[23] H. Yu-Fen, H. Kuan-Ming, C. Huan-Tsung, *J. Colloid Interface Sci.* **2006**, *301*, 145–154.
[24] I. Halaciuga, D. V. Goia, *J. Mater. Res.* **2008**, *23*, 1776–1784.
[25] D. Andreescu, T. K. Sau, D. V. Goia, *J. Colloid Interface Sci.* **2006**, *298*, 742–751.
[26] A. Henglein, M. Giersig, *J. Phys. Chem. B* **1999**, *103*, 9533–9539.
[27] Z. S. Pillai, P. V. Kamat, *J. Phys. Chem. B* **2004**, *108*, 945–951.
[28] A. Mantion, A. G. Guex, A. Foelske, L. Mirolo, K. M. Fromm, M. Painsi, A. Taubert, *Soft Matter* **2008**, *4*, 606–617.
[29] E. E. Foos, A. W. Snow, M. E. Twigg, M. G. Ancona, *Chem. Mater.* **2002**, *14*, 2401–2408.
[30] S.-W. Kim, S. Kim, J. B. Tracy, A. Jasanoff, M. G. Bawendi, *J. Am. Chem. Soc.* **2005**, *127*, 4556–4557.
[31] S. Kéki, J. Török, G. Deák, L. Daróczi, M. Zsuga, *J. Colloid Interface Sci.* **2000**, *229*, 550–553.
[32] A. H. Latham, M. E. Williams, *Langmuir* **2006**, *22*, 4319–4326.
[33] A. Manna, T. Imae, K. Aoi, M. Okada, T. Yogo, *Chem. Mater.* **2001**, *13*, 1674–1681.
[34] U. Oktay, H. Ying, V. Ayush, C. Suelin, C. Andrea, S. Francesco, *Chem. Commun.* **2007**, 196–198.
[35] D. I. Gittins, F. Caruso, *ChemPhysChem* **2002**, *3*, 110–113.
[36] C. H. B. Ng, J. Yang, W. Y. Fan, *J. Phys. Chem. C* **2008**, *112*, 4141–4145.
[37] R. M. Kramer, C. Li, D. C. Carter, M. O. Stone, R. R. Naik, *J. Am. Chem. Soc.* **2004**, *126*, 13282–13286.
[38] S. Banta, Z. Megeed, M. Casali, K. Rege, M. L. Yarmush, *J. Nanosci. Nanotechnol.* **2007**, *7*, 387–401.
[39] K. Channon, C. E. MacPhee, *Soft Matter* **2008**, *4*, 647–652.
[40] S. S. Santoso, S. Zhang, *Encycl. Nanosci. Nanotechnol.* **2004**, 459–471.
[41] R. R. Naik, S. J. Stringer, G. Agarwal, S. E. Jones, M. O. Stone, *Nat. Mater.* **2002**, *1*, 169–172.
[42] S. Si, E. Dinda, T. Mandal, *Chem. Eur. J.* **2007**, *13*, 9850–9861.
[43] S. Si, T. K. Mandal, *Chem. Eur. J.* **2007**, *13*, 3160–3168.
[44] S. Ray, A. K. Das, A. Banerjee, *Chem. Commun.* **2006**, 2816–2818.
[45] M. Brust, J. Fink, D. Bethell, D. J. Schiffrin, C. Kiely, *J. Chem. Soc. Chem. Commun.* **1995**, 1655–1656.
[46] M. Brust, M. Walker, D. Bethell, D. J. Schiffrin, R. Whyman, *J. Chem. Soc. Chem. Commun.* **1994**, 801–802.
[47] M. Haupt, S. Miller, R. Glass, M. Arnold, R. Sauer, K. Thonke, M. Moller, J. P. Spatz, *Adv. Mater.* **2003**, *15*, 829–831.
[48] R. R. Naik, S. E. Jones, C. J. Murray, J. C. McAuliffe, R. A. Vaia, M. O. Stone, *Adv. Funct. Mater.* **2004**, *14*, 25–30.
[49] A. Semenov, J. P. Spatz, M. Moller, J.-M. Lehn, B. Sell, D. Schubert, C. H. Weidl, U. S. Schubert, *Angew. Chem.* **1999**, *111*, 2701–2705; *Angew. Chem. Int. Ed.* **1999**, *38*, 2547–2550.
[50] J. P. Spatz, S. Mossmer, M. Moller, T. Herzog, A. Plettl, P. Ziemann, *Polym. Mater. Sci. Eng.* **1997**, *77*, 420–421.
[51] Q. Dong, H. Su, D. Zhang, *J. Phys. Chem. B* **2005**, *109*, 17429–17434.
[52] R. Lévy, K. T. Thanh Nguyen, D. R. Christopher, H. Irshad, R. J. Nichols, D. J. Schiffrin, M. Brust, D. G. Fernig, *J. Am. Chem. Soc.* **2004**, *126*, 10076–10084.
[53] J. Slocik, D. Wright, *Biomacromolecules* **2003**, *4*, 1135–1141.
[54] Z. Wang, R. Lévy, D. G. Fernig, M. Brust, *Bioconjugate Chem.* **2005**, *16*, 497–500.
[55] J. Kong, S. Yu, *Acta Biochim. Biophys. Sin.* **2007**, *39*, 549–559.
[56] H. Maekawa, C. Toniolo, A. Moretto, Q. Broxterman, N.-H. Ge, *J. Phys. Chem. B* **2006**, *110*, 5834–5837.
[57] G. Martinez, G. Millhauser, *J. Struct. Biol.* **1995**, *114*, 23–27.
[58] A. Mantion, A. Taubert, *Macromol. Biosci.* **2007**, *7*, 208–217.
[59] S. Y. Venyaminov, N. N. Kalnin, *Biopolymers* **1990**, *30*, 1243–1257.
[60] L. Pauling, R. B. Corey, H. R. Branson, *Proc. Natl. Acad. Sci. USA* **1951**, *37*, 205–211.
[61] M. A. Van Hove, G. A. Somorjai, *Surfactant Sci. Ser.* **1980**, *92*, 489–518.
[62] P. D. Jadzinsky, G. Calero, C. J. Ackerson, D. A. Bushnell, R. D. Kornberg, *Science* **2007**, *318*, 430–433.
[63] C. Gautier, T. Buergi, *J. Am. Chem. Soc.* **2008**, *130*, 7077–7084.
[64] J. Rodríguez-Carvajal, *Physica B+C* **1993**, *192*, 55–69.
[65] C. J. Sandroff, D. R. Herschbach, *J. Phys. Chem.* **1982**, *86*, 3277–3279.

  

[66] B. Pettinger, H. Wetzel, *Chem. Phys. Lett.* **1981**, *78*, 398–403.
[67] B. A. Sexton, R. J. Madix, *Chem. Phys. Lett.* **1980**, *76*, 294–297.
[68] M. Schnippering, M. Carrara, A. Foelske, R. Kötz, D. J. Fermín, *Phys. Chem. Chem. Phys.* **2007**, *9*, 725–730.
[69] G. Faraci, E. Costanzo, A. R. Pennisi, Y. Hwu, G. Margaritondo, *Z. Phys. D: At. Mol. Clusters* **1992**, *23*, 263–267.
[70] L. Guczi, G. Peto, A. Beck, Z. Paszti, *Curr. Top. Catal.* **2004**, *29*, 129–138.
[71] H. S. Shina, H. C. Choia, Y. Junga, S. B. Kim, H. J. Song, H. J. Shin, *Chem. Phys. Lett.* **2004**, *383*, 418–422.
[72] K. Ashavani, J. Hrushikesh, P. Renu, M. A. B. S. Murali, *J. Colloid Interface Sci.* **2003**, *264*, 396–401.
[73] S. Kang, K. Kim, *Langmuir* **1998**, *14*, 226–230.
[74] C. D. Wagner, G. E. Muilenberg, *Handbook of X-ray photoelectron spectroscopy: A reference book of standard data for use in x-ray photoelectron spectroscopy*, Perkin-Elmer, Eden Prairie, **1979**, p. 122.
[75] C.-J. Zhong, M. D. Porter, *J. Am. Chem. Soc.* **1994**, *116*, 11616–11617.
[76] L. D. Setiawan, H. Baumann, D. Gribbin, *Surf. and Interface Anal.* **1985**, *7*, 188–195.
[77] J. C. Munro, C. W. Frank, *Polymer* **2003**, *44*, 6335–6344.
[78] L. M. Sigg, W. Stumm, *Aquatische Chemie*, Teubner, Stuttgart, **1994**.
[79] K. Kelly, E. Coronado, L. Zhao, G. Schatz, *J. Phys. Chem. B* **2003**, *107*, 668–677.
[80] J. J. Mock, M. Barbic, D. R. Smith, D. A. Schultz, S. Schultz, *J. Chem. Phys.* **2002**, *116*, 6755–6759.
[81] I. Sosa, C. Noguez, R. Barrera, *J. Phys. Chem. B* **2003**, *107*, 6269–6275.
[82] M. Brust, C. J. Kiely, *Colloids Surf. A* **2002**, *202*, 175–186.
[83] Y.-S. Shon, D. Choi, *Curr. Nanosci.* **2007**, *3*, 245–254.
[84] L. C. Gruen, *Biochim. Biophys. Acta* **1975**, *386*, 270–274.
[85] N. Naoki, Y. Hiroshi, K. Keisaku, *Langmuir* **2008**, *24*, 2759–2766.
[86] J. I. Pascual, J. V. Barth, G. Ceballos, G. Trimarchi, A. De Vita, K. Kern, H.-P. Rust, *J. Chem. Phys.* **2004**, *120*, 11367–11370.
[87] G. Shemer, O. Krichevski, G. Markovich, T. Molotsky, I. Lubitz, A. B. Kotlyar, *J. Am. Chem. Soc.* **2006**, *128*, 11006–11007.
[88] C. M. Niemeyer, B. Ceyhan, S. Gao, L. Chi, S. Peschel, U. Simon, *Colloid Polym. Sci.* **2001**, *279*, 68–72.
[89] M. Wanner, D. Gerthsen, S.-S. Jester, B. Sarkar, B. Schwederski, *Colloid Polym. Sci.* **2005**, *283*, 783–792.
[90] J. Xie, J. Y. Lee, D. I. C. Wang, Y. P. Ting, *ACS Nano* **2007**, *1*, 429–439.
[91] P. Thompson, D. E. Cox, J. B. Hastings, *J. Appl. Crystallogr.* **1987**, *20*, 79–83.
[92] D. Louër, J. I. Langford, *J. Appl. Crystallogr.* **1988**, *21*, 430–437.
[93] J. Rodriguez-Carvajal, M. T. Fernandez-Diaz, J. L. Martinez, *J. Phys. Condens. Matter* **1991**, *3*, 3215–3234.
[94] M. Jarvinen, *J. Appl. Crystallogr.* **1993**, *26*, 525–531.
[95] P. B. Johnson, R. W. Christy, *Phys. Rev. B* **1972**, *6*, 4370–4379.
[96] D. Pontoni, S. Finet, T. Narayanan, A. R. Rennie, *J. Chem. Phys.* **2003**, *119*, 6157–6165.
[97] R. V. Sharman, K. C. Sharman, *Physica* **1977**, *89*, 213–217.

Received: November 9, 2008
Revised: February 6, 2009
Published online: April 15, 2009

  